2023

Effects of silicon dioxide as the polar dielectric on the infrared absorption spectrum ofthemetal-insulator-metal metasurface

Ahmad K. Jafari

Matthew Gaddy

Imtiaz Ahmad

Satya R. Kachiraju

M D. Borhan Mia

See next page for additional authors

Authors

Ahmad K. Jafari, Matthew Gaddy, Imtiaz Ahmad, Satya R. Kachiraju, M D. Borhan Mia, Ishtiaque Ahmed, Sergey Nikishin, Myoung-Hwan Kim, and Ayrton A. Bernussi

Effects of silicon dioxide as the polar dielectric on the infrared absorption spectrum of the metal-insulator-metal metasurface

To cite this article: Ahmad K Jafari *et al* 2023 *Mater. Res. Express* **10** 015801

Materials Research Express

PAPER

Effects of silicon dioxide as the polar dielectric on the infrared absorption spectrum of the metal-insulator-metal metasurface

Ahmad K Jafari[1,3,*], **Matthew Gaddy**[2,3], **Imtiaz Ahmad**[1], **Satya R Kachiraju**[1,4], **M D Borhan Mia**[2], **Ishtiaque Ahmed**[1,3], **Sergey Nikishin**[2,3], **Myoung-Hwan Kim**[1] and **Ayrton A Bernussi**[2,3]

[1] Department of Physics and Astronomy, Texas Tech University, Lubbock, TX 79409, United States of America
[2] Department of Electrical and Computer Engineering, Texas Tech University, Lubbock, TX 79409, United States of America
[3] Nano Tech Center, Texas Tech University, Lubbock, TX 79409, United States of America
[4] Department of Physics and Astronomy, University of Texas Rio Grande Valley, Brownsville, TX, 78520, USA, United States of America
[*] Author to whom any correspondence should be addressed.

E-mail: ahmad.jafari@ttu.edu

Keywords: metal-insulator-metal metasurafces, mid-infrared, polar dielectrics, berreman mode, epsilon-near-zero mode

OPEN ACCESS

RECEIVED
19 September 2022

REVISED
26 December 2022

ACCEPTED FOR PUBLICATION
30 December 2022

PUBLISHED
11 January 2023

Abstract

Metal-insulator-metal metasurfaces have been widely used as high-performance absorbers in almost all electromagnetic spectral ranges. Their absorption spectra can be engineered by making variations in the geometry of the unit cells and/or by embedding materials with specific optical constants. Including a polar dielectric in their structure is another approach for manipulating their absorption spectra. In this research, we have numerically and experimentally investigated the effect of using silicon dioxide (SiO_2) as a polar dielectric on the absorption spectrum of a metal-insulator-metal metasurface composed of a tri-layer of *Ni-*SiO_2*-Ni*. Our results have shown the presence of absorption peaks in the mid-infrared which are attributed to the excitation of the optical phonons in the SiO_2 spacer layer. Particularly, the excitation of the Berreman mode in the SiO_2 spacer layer was observed and its effect on the total absorption spectrum is studied. The parametric effects of the top patterned *Ni* layer, the incident angle, and the polarization are also investigated. This study can provide engineering capabilities for the mid-infrared absorbers and reflection filters.

1. Introduction

Among different high-performance absorber designs, metal-insulator-metal metasurfaces (*MIM-M*) are of particular importance because they strongly interact with the incident electromagnetic field in the near-field region and can completely absorb the incident radiation. A typical *MIM-M* consists of a uniform metallic backplane layer, an intermediate uniform insulating layer, and an array of periodic thin metallic structures lithographically patterned atop [1–3]. Extensive studies have shown that *MIM-M*s are excellent absorbers in the visible (*VIS*) and the near-infrared (*NIR*) with the ability to tune the absorption peaks spectrally and spatially [3]. The origin of high absorption in these structures is attributed to the excitation of a variety of electromagnetic resonances which, in turn, results in the strong confinement of the electromagnetic energy in the gap between the top metallic patterned layer and the metallic backplane layer [4]. The absorption wavelength and its bandwidth can be tuned by varying the dimensions of the unit cells as well as the constituent materials with specific optical constants [5–7]. Also, external stimuli such as heat [8] can cause considerable nonlinear optical absorption in these structures. *MIM-M*s have inspired the realization of devices in the field of photonics and plasmonics including detectors [9, 10], novel energy harvesting devices [11], ultrathin flat lenses [12], imaging [13], resonant enhancement of Raman scattering [14], and on-chip integration [1].

MIR is a spectral region of tremendous scientific and technological interest as the vibrational transitions of many important molecules exist in this spectral region making *MIR* photonic devices crucial for applications in chemical and biomolecular sensing and spectroscopy [10, 15, 16]. Recently, polar dielectrics such as silicon dioxide (SiO_2), silicon carbide (*SiC*), gallium phosphide (*GaP*), and gallium nitride (*GaN*) have attracted much

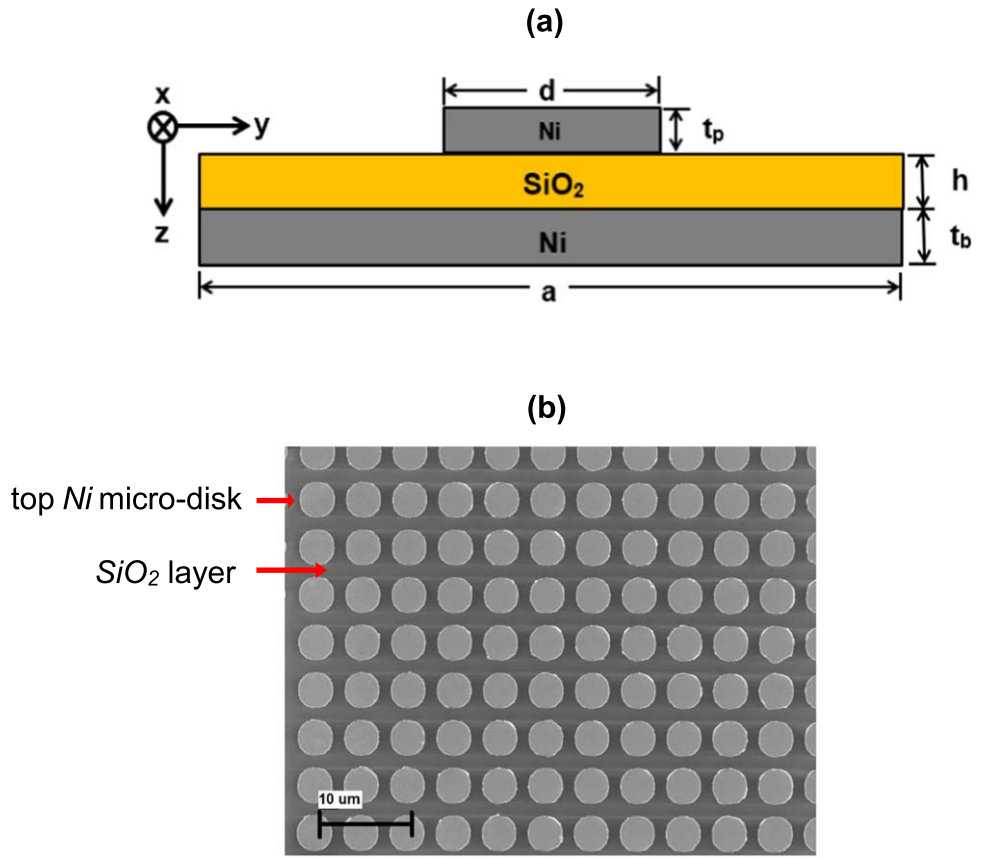

Figure 1. (a) Schematic side view of *Ni/SiO$_2$/Ni* tri-layer metasurface unit cell (not to scale). (b) The *SEM* image of a fabricated *MIM-M* sample with $a = 5$ μm and $d = 4$ μm. Circles (gray) show the top *Ni* micro-disks on top of the *SiO$_2$* uniform layer (black). Other parameters are fixed to $t_p = 50$ nm, $h = 300$ nm, $t_b = 100$ nm. Scale bar indicates 10 μm.

attention as insulating materials platform which can manipulate light–matter interaction in the mid-infrared (*MIR*) region [16–18]. It is possible to excite optical phonon waves in polar dielectrics with their negative real and positive imaginary parts of permittivity in the *MIR* region. Under specific excitation conditions, the incident radiation can excite surface waves in polar dielectrics known as surface phonon polaritons (*SPhP*s). This is analogous to its counterpart in metals named the surface plasmon polaritons (*SPP*s). The excitation of the optical phonon waves in polar dielectrics has been extensively studied both theoretically [19, 20] and experimentally [17, 21, 22]. However, the use of polar dielectrics in the *MIM-M*s is not fully explored yet and new and rich physics could be explored by including polar dielectrics *MIM-M*s [22, 23].

In this paper, we numerically and experimentally studied Nickel (*Ni*)-based *MIM-M*s encompassing *SiO$_2$* as the polar dielectric (*Ni-SiO$_2$-Ni* tri-layer structure). Two different optical phonon resonances known as the Berreman (*BE*) [23–25] and epsilon-near-zero (*ENZ*) [26–29] modes are excited, and they are utilized to engineer the absorption spectrum in the *MIR* region. We have also investigated the interaction between the plasmonic resonances (from the metallic structures) and the *BE* mode (from the polar dielectric *SiO$_2$* spacer) and found that the *BE* mode suppresses the plasmonic resonances in a way that they can't be excited simultaneously. In order to fully exploring the engineering capabilities of our proposed *MIM-M*, the effects of the top *Ni* pattern dimensions, lattice constant, incident angle, and its polarization on the absorption spectra were also studied.

2. Structure and absorption simulation

A schematic illustration of the proposed *MIM-M* unit cell is shown in figure 1(a). The *MIM-M* consists of a stack of three layers: a bottom uniform *Ni* layer, a *SiO$_2$* spacer layer, and the top *Ni* micro-disks. The geometrical parameters of the unit cell consist of the diameter of the *Ni* micro-disk (d) and its thickness (t_p), the thickness of the *SiO$_2$* spacer layer (h) and the lattice constant of the structure (a), i.e., the periodicity. The thickness of the bottom *Ni* layer ($t_b = 100$ nm) which is much larger than its skin depth (approximately 45 nm for *Ni* in the spectral range of 5–12 μm) prevents electromagnetic wave transmission. We chose to use *Ni* as a metal, as it shows a high melting point which is ideal for energy harvesting applications such as solar thermophotovoltaic

(*STPV*) systems [6]. *Ni* is also ferromagnetic; thus, it has the potential to couple plasmonic resonance with its magnetic properties [30].

The simulations were carried out in the frequency domain by utilizing the Wave Optics Module of the commercial software COMSOL Multiphysics®. The periodicities of the unit cell in both *x*- and *y*-direction were set by the Floquet boundary conditions. Plane waves impinge upon the unit cell and the reflection and transmission are monitored. A perfectly matched layer (*PML*) absorbing boundary condition has been employed along the *z*-direction (the propagation direction).

3. Sample fabrication and experimental characterization

As previously described, our proposed *MIM-M* consists of three layers: a bottom *Ni* layer, a middle SiO_2 layer, and top periodic micro-structured *Ni* disks. The *MIM-M* samples have been fabricated by depositing a 100-nm-thick *Ni* layer on top of a Silicon (Si) wafer using electron beam deposition (*EBD*). *The* SiO_2 layer was then deposited using plasma-enhanced chemical vapor deposition (*PE-CVD*). An *S1813* resist mask is patterned for the deposition of the top micro-disk array by deep *UV* lithography and a photomask. The final 50-nm-thick *Ni* layer was deposited by the *EBD* followed by lift-off in acetone. A scanning electron microscope (*SEM*) image of one of the fabricated samples ($a = 5\ \mu$m and $d = 4\ \mu$m) is shown in figure 1(b). Since the incident beam size on the samples becomes elongated and large at oblique incidences, we fabricated all samples as large as 1 cm by 1 cm using deep *UV* lithography. This large size sample helped to focus the light exactly on the sample even at the incident angle $\theta_i = 60°$.

The characterization of the samples involves reflection measurements utilizing the Fourier transform infrared (*FT-IR*) spectroscopy. An external Globar radiation source (550 nm–15 μm) illuminated the samples at normal or oblique incidence. The reflected light from the samples was collected and steered into the *FT-IR* (Bruker VERTEX 70*v*). A wire grid polarizer (ThorLabs, *KRS*-5), which operates in the range of 2–30 μm with an extinction ratio of 300:1, has been mounted in front of the radiation source to distinguish between transverse magnetic (*TM*)- and transverse electric (*TE*)-polarized modes. It also allows having a mix of *TM*- and *TE*-modes by rotating its wire grid axis. All the measurements were normalized to a reference gold mirror (ThorLabs, *PF10–03-M01*).

4. Results and discussion

Figure 2(a) illustrates schematic setup used in the reflectance measurements by the *FT-IR* where φ is the rotation angle of the linear polarizer (*TM:* $\varphi = 180°$, and *TE:* $\varphi = 90°$) and θ_i is the radiation incident angle. Due to zero transmission, reflectance dips in these spectra correspond to absorptance peaks (Absorptance = 1- Reflectance). Figure 2(b) shows the dispersion of the real and imaginary parts of the permittivity of the SiO_2 [31]. Having an absorption band in the *MIR* spectral region for the SiO_2 means that the real part of its permittivity becomes zero ($\varepsilon_r = 0$) and negative ($\varepsilon_r < 0$) whereas the imaginary part becomes positive ($\varepsilon_i > 0$) [32]. The crossing point between the positive ε_r and the negative ε_r where $\varepsilon_r = 0$ is known as the *ENZ* mode. The *ENZ* mode which is a local electric field confinement occurs because the normal component of the electric field E_{normal} is both enhanced and confined due to the continuity of εE_{normal} at the interfaces [21]. Also, it can be noticed from figure 2(b) that in the wavelength range of 7.8 μm $\leqslant \lambda \leqslant$ 10.9 μm the imaginary part of permittivity of SiO_2 has a positive value which implies an absorption in this range. This is the spectral region where the *BE* mode (which is a longitudinal optical phonon mode) is excited by the *TM*- polarized radiation. The point where the imaginary part of the permittivity has a peak is known as the epsilon-near-pole (*ENP*) [33]. It is worth mentioning the importance of highly absorbing dielectric films which can be prospectively used as ultrathin photodetectors and solar cells [34]. *BE* and *ENZ* are two modes of excitations with different physical mechanisms [21]. While the *BE* mode is a leaky mode which can propagate [25], the *ENZ* is a non-radiative mode which is confined close to the interface [21]. By depositing a thin layer of SiO_2 on metallic films these excitations become more pronounced [19, 20, 23].

MIM-M is a structure used for studying and manipulating the gap-surface plasmon (*GSP*) modes [1, 4]. By embedding a polar dielectric such as SiO_2 as a spacer in a *MIM-M*, it is possible to study the *GSP* and the *BE* modes together and probe the interaction between these two excitations. In fact, we have used a patterned structure (micro-disk on top of the SiO_2 as a polar dielectric) to explore the excitation of the *BE* mode alongside probing its interaction with the *GSP* mode.

For the sake of comparison, the simulation and experimental results for the reflectance spectra of a layer of SiO_2 on Ni layer without any patterning on top of the SiO_2 layer is shown in figures 2(c) and (d). The effects of the incident angle and polarization on the reflectance spectra of SiO_2/*Ni* structure (the thicknesses of SiO_2 and *Ni* are fixed at 300 nm and 100 nm, respectively) are shown in these figures. Figure 2(c) shows a comparison between

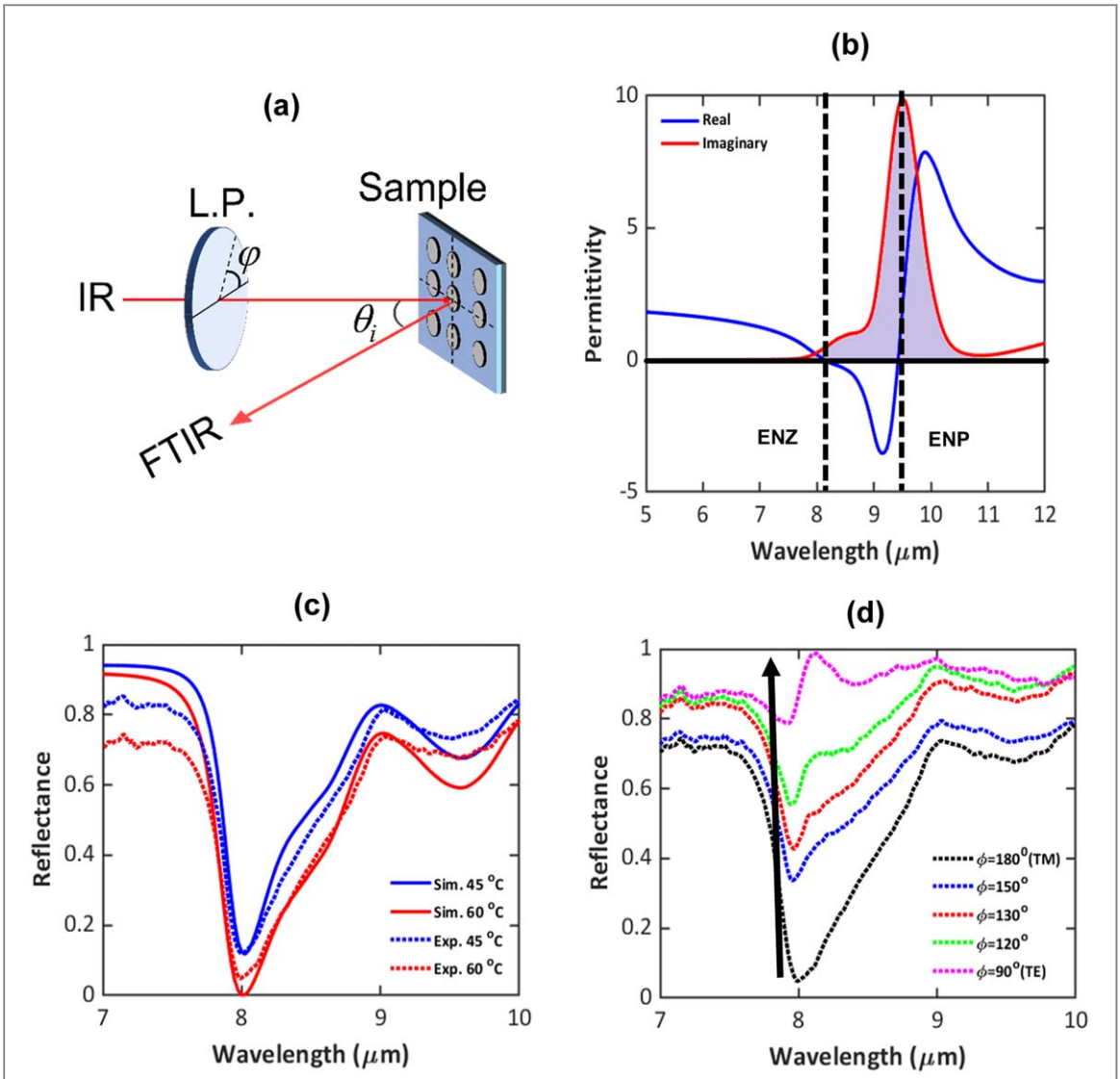

Figure 2. (a) Schematic of the experimental reflectance setup: φ is the polarization rotation angle of the linear polarizer (*LP*) and θ_i is the *IR* light incident angle at the surface of the *MIM-M* sample. (b) Permittivity of SiO_2 which shows the *ENZ* at 8.2 μm and the *ENP* at 9.5 μm. The absorption peak starts from 7.6 μm end ends at 10.6 μm (shaded area) [22]. (c) Simulated and measured reflectance spectra of SiO_2/*Ni* structure at $\theta_i = 45^\circ$ and $\theta_i = 60^\circ$. (d) Experimental reflectance measurement for SiO_2/*Ni* structure as the incident light polarization changes from *TM* to *TE* (the direction of the arrow). The polarizer angle φ for each case is also shown.

simulated and measured reflectance spectra for *TM* polarization for $\theta_i = 45^\circ$ and $\theta_i = 60^\circ$. In addition to the reflectance dip at the $\lambda \approx 8$ μm (*BE* mode), there is another dip centered at the $\lambda \approx 9.5$ μm. The latter reflectance dip is the *ENP* point [see figure 2(b)]. Figure 2(d) depicts the reflectance spectra as the incident polarization changes from the *TM*- to the *TE*-mode. As the incident polarization varies towards the *TE*-mode, the amplitude of the reflectance dip associated with the *BE* mode reduces till there is no dip for the *TE*-mode. The polarizer rotation angle is also shown for each case.

For *MIM-M* samples, the thickness of the SiO_2 spacer layer has been fixed to $h = 300$ nm in all structures which is the same as for the unpatterned structure. Based on our simulations, this thickness causes the best impedance match between air and the *MIM-M*. The lattice constant was fixed at $a = 5$ μm and different top micro-disks' diameter ($d_1 = 3$ μm, $d_2 = 3.5$ μm, and $d_3 = 4$ μm) were fabricated. Measured and simulated reflectance spectra at normal incidence are shown in figure 3(a). From this figure, it is clear that as the diameter of the micro-disk increases, the *GSP* mode shifts to longer wavelengths. The reflectance dip varies from $\lambda_1 \approx 7.6$ μm to $\lambda_3 \approx 7.8$ μm as the top micro-disk diameter was varied from 3 μm to 4 μm, respectively (red-shift) [4]. Measured reflectance spectra for the sample with $a = 5$ μm and $d = 3.0, 3.5, 4.0$ μm at $\theta_i = 45^\circ$ and for *TM*-mode are illustrated in figure 3(b). The reflectance dips due to the *BE* mode at $\lambda \approx 8$ μm is the dominant feature in the *TM*-polarized reflectance spectra for all samples. As the diameter of the micro-disk increases, the reflection dips associated with the *GSP* mode shifts to longer wavelengths and becomes closer to the *BE* mode. Figure 3(c) shows a comparison between simulated and measured reflectance spectra for one the samples ($a = 5$ μm and

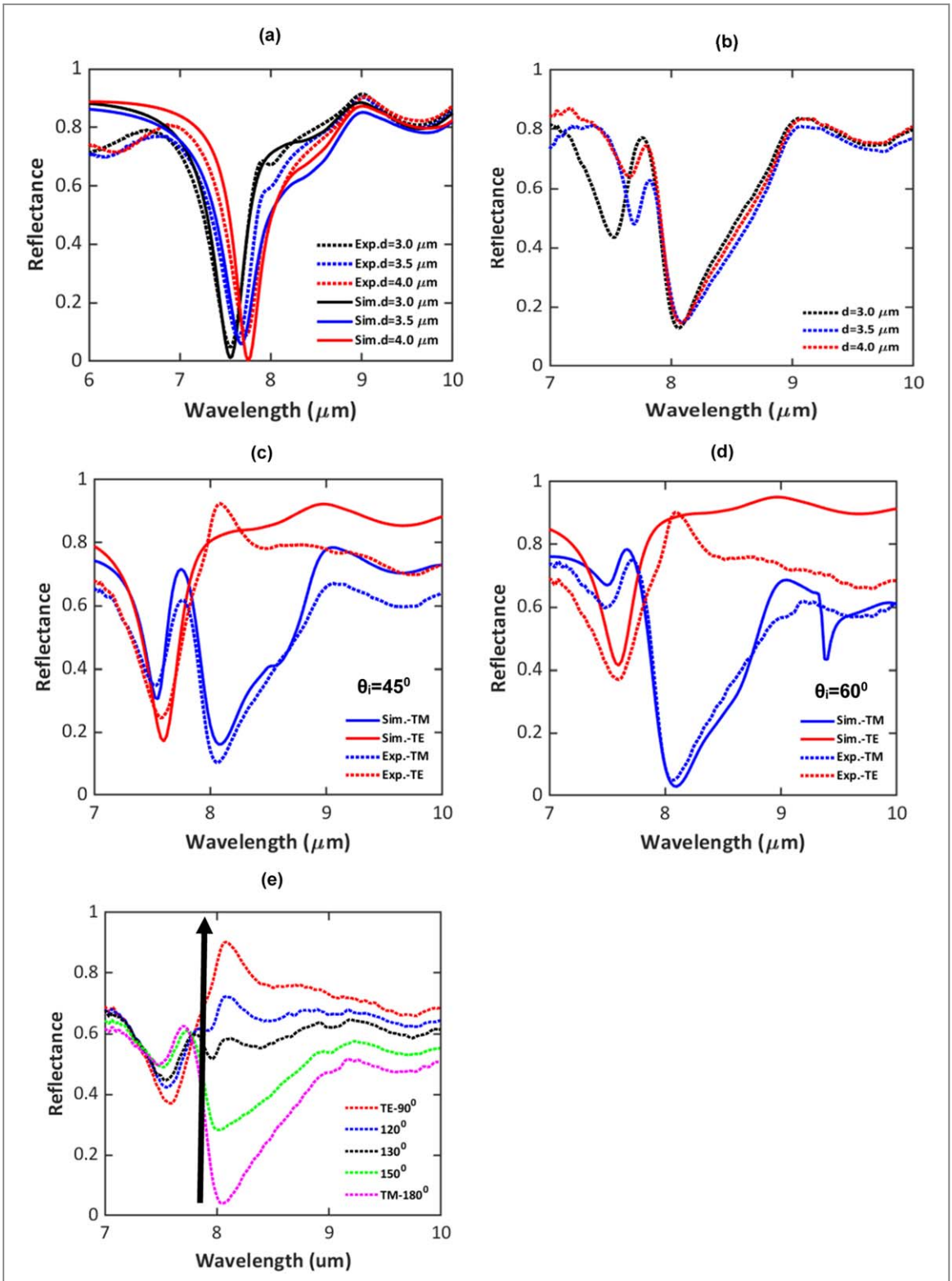

Figure 3. (a) Simulated and measured reflectance spectra for *Ni/SiO$_2$/Ni* samples at normal incidence ($\theta_i = 0°$) for samples with $a = 5$ μm and $d = 3.0$, 3.5, and 4.0 μm. (b) Measured reflectance spectra for *Ni/SiO$_2$/Ni* samples with $a = 5$ μm, and $d = 3.0$, 3.5, 4.0 μm for the *TM*-mode at (c) $\theta_i = 45°$, and (d) $\theta_i = 60°$. (e) Experimental measurements of the *Ni/SiO$_2$/Ni* sample with $a = 5$ μm and $d = 3$ μm as the incident light polarization changes from *TM* to *TE* (the direction of the arrow).

$d = 3.5$ μm) for both *TM*- and *TE*- modes. Simulated and measured reflectance spectra for the sample with $a = 5$ μm and $d = 3.5$ at $\theta_i = 60°$ for *TM*-mode are illustrated in figure 4(d). As it is observed, the amplitude of the reflectance dip due to the *BE* mode enhances more compared with $\theta_i = 45°$. From the experimental measurements, the amplitude of the reflectance dip due to the *BE* mode reaches its maximum at $\lambda \approx 8$ μm which is 8% reflectance (92% absorptance). Figure 3(e) depicts the change of reflectance as the incident polarization changes from the *TM*- to the *TE*-mode for the aforementioned sample. Similar to the unpatterned structure, by

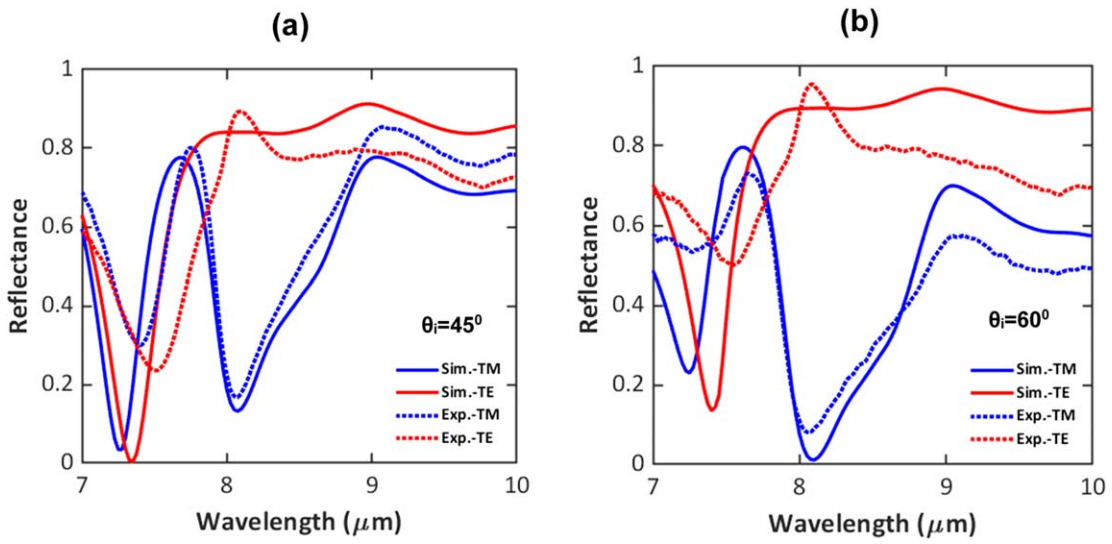

Figure 4. Experiment and simulation for *Ni/SiO₂/Ni* samples with $a = 4\ \mu$m and $d = 3\ \mu$m at *TM*- and *TE*-modes: (a) $\theta_i = 45°$, and (b) $\theta_i = 60°$.

changing the polarization from the *TM*-mode to the *TE*-mode, the amplitude of the reflectance dip associated with the *BE* mode reduces. By comparing the incident wavelength range (5 μm to 12 μm) for the samples with $a = 5\ \mu$m, it turns out that the diffraction losses become significant at high oblique incident angles. One possible approach to minimize the influence of the diffraction losses is to implement the random structure. In this type of structure, the top metallic patches are the same size, but they are arranged in random positions on top of the dielectric spacer layer [35]. Another approach is to decrease the lattice constant in a way that it becomes quite shorter than the minimum incident light wavelength. Figures 4(a) and (b) shows the reflectance measurements and simulation results for the structure with $a = 4\ \mu$m and $d = 3.5\ \mu$m at $\theta_i = 45°$ and $\theta_i = 60°$, respectively. Compared with the previous cases ($a = 5\ \mu$m), the diffraction orders from the structure are less accentuated and the reflection dips become wider, particularly for $\theta_i = 60°$. The observed differences between simulated and experimental spectra occur mostly due to the sample fabrication process which leads to deviations from the original design. Additionally, comparing the *TM*- and *TE*- mode reflection spectra for the *MIM-M*s shows that for *TM*-mode, the reflection dips associated with the *GSP* mode decrease and are also suppressed compared with the *TE*-mode. This occurs due to the emergence of the *BE* mode at the $\lambda \approx 8\ \mu$m [20–22]. In addition to the fabrication issues, another possible source of error can be associated with the wavelength dispersion of the permittivity used in our simulations which might slightly differ from those of the fabricated samples.

By comparing the results from the unpatterend (*SiO₂/Ni*) and patterned (*Ni/SiO₂/Ni*) structures, it is concluded that the *BE* mode is always excited even with having the periodic *Ni* pattern above the *SiO₂* layer. On the other hand, the top *Ni* pattern causes the two distinct modes (*BE* and *ENP*) to merge into each other and makes the reflectance dip wider. This dip (37% absorptance at $\theta_i = 60°$ for the *TM*-mode) is merged in the dip originated from the *BE* mode for the *MIM-M* reflectance spectra.

For any *MIM-M*, there are three different contributions to the total absorption: (1) the continuous metallic backplane layer, (2) the periodic metallic patterns, and (3) the dielectric layer [23]. Previous studies have only investigated the total absorption without any study of the contribution of the different layers. In order to calculate each individual absorption contribution, we computed the integrated absorbed power for each region of the *MIM-M*. Figures 5(a) and (b) illustrate the contribution of each layer to the total reflection dip for the sample with $a = 5\ \mu$m and $d = 3.5\ \mu$m at $\theta_i = 60°$ for *TM*- and *TE*-modes, respectively. From these figures, it is clearly seen that for both *TM*- and *TE*-modes at the wavelength range where the imaginary part of the permittivity of the *SiO₂* becomes positive the contribution from the *GSP* mode falls to zero. While the *BE* mode is excited in this range for the *TM*-mode and the absorption from the *SiO₂* spacer layer becomes dominant, the *TE*-mode shows low absorption (less than 10%). Other geometries also exhibited very similar trends. This is a direct consequence of the fact that as the real part of the permittivity of the *SiO₂* becomes negative [see figure 2(b)], any absorption due to plasmonic excitation falls to zero and only the absorption from the *SiO₂* layer becomes dominant. The condition for having any plasmonic resonance is that the metallic layer has a negative real permittivity whereas the insulator layer in contact with it should have a positive permittivity [36]. Hence, the two aforementioned absorption modes cannot be excited at the same wavelength (there is no interaction between them) although by appropriate design they can be very close to each other [37, 38]. For the *TE*-mode,

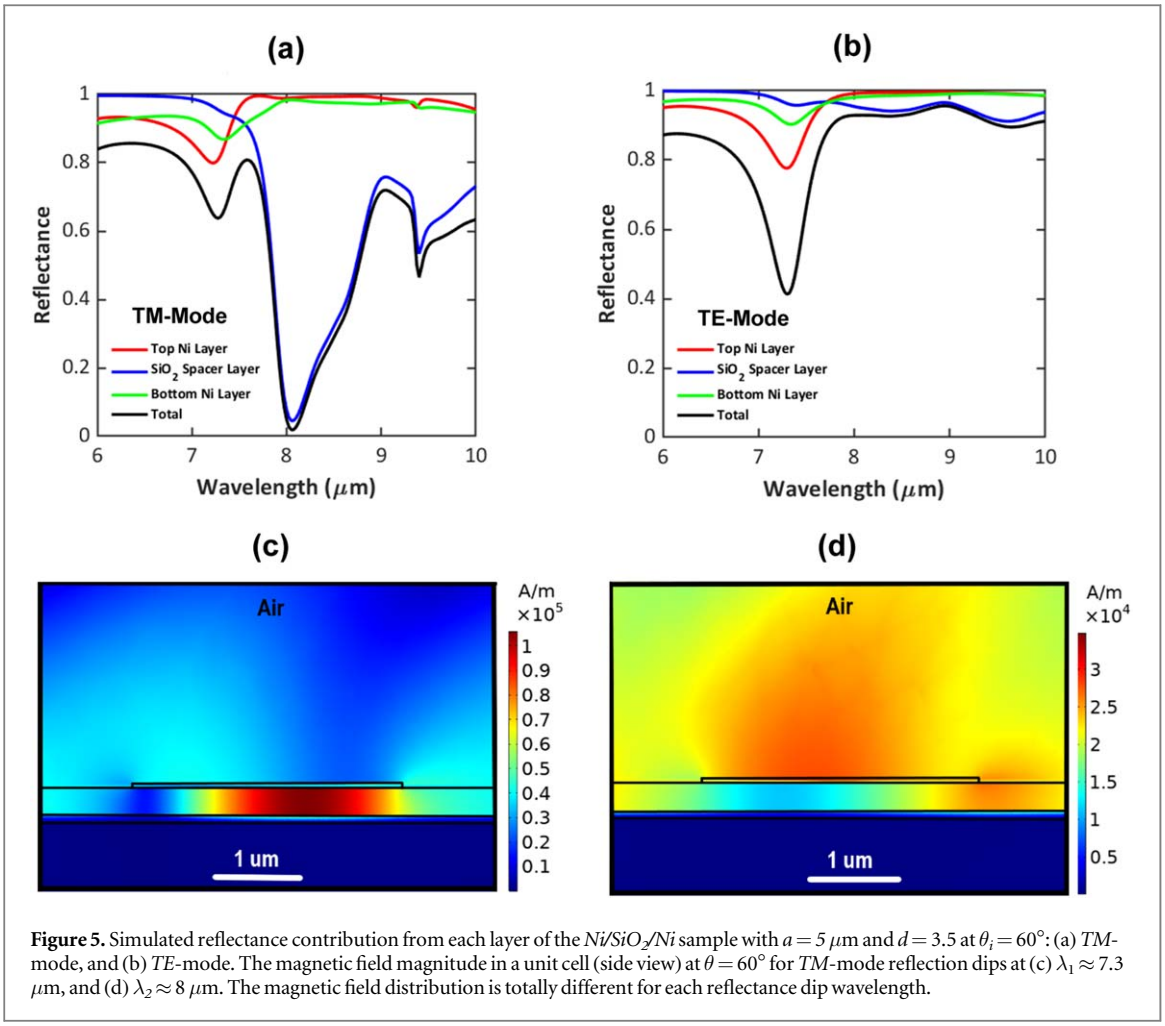

Figure 5. Simulated reflectance contribution from each layer of the *Ni/SiO$_2$/Ni* sample with $a = 5$ μm and $d = 3.5$ at $\theta_i = 60°$: (a) *TM*-mode, and (b) *TE*-mode. The magnetic field magnitude in a unit cell (side view) at $\theta = 60°$ for *TM*-mode reflection dips at (c) $\lambda_1 \approx 7.3$ μm, and (d) $\lambda_2 \approx 8$ μm. The magnetic field distribution is totally different for each reflectance dip wavelength.

any absorption related to the *SiO$_2$* spacer layer is only associated to the *ENZ* mode. Figures 5(c) and (d) illustrates the *TM*-mode magnetic field intensity (*H*-field) distribution inside the *MIM-M* at the two main reflection dips for the structure with $a = 5$ μm and $d = 3.5$ μm at $\theta_i = 60°$. For $\lambda \approx 7.3$ μm the magnetic field is mainly concentrated within the gap between the top *Ni* micro-disks and the bottom *Ni* layer. This is direct evidence that these reflection dips correspond to the *GSP* excitation, and the absorption occurs only due to the top *Ni* micro-disks and the bottom *Ni* film [4]. However, at $\lambda \approx 8$ μm, no magnetic field enhancement is observed which indicates that at this wavelength the *GSP* excitation does not happen and the absorption inside the *SiO$_2$* spacer layer occurs merely due to the *BE* mode excitation.

5. Conclusions

In this research, the reflectance spectra of *MIM-M*s encompassing a polar dielectric (*SiO$_2$*) have been investigated both numerically and experimentally in the *MIR* region where the optical phonon waves in the *SiO$_2$* spacer are excited. The effects of varying the size of the top metallic layer, lattice constant, and the radiation incident angle and its polarization on the reflection spectra have been studied in detail. It has been demonstrated that all the three layers of the *MIM-M*s contribute differently to the reflection spectra at normal and oblique incidences. However, in a wavelength range at which the real part of the permittivity of the *SiO$_2$* spacer layer is negative, no plasmonic mode is excited whereas the *BE* mode comes into play, and this means that the plasmonic and the *BE* modes cannot be excited simultaneously. This research is important in the fields of thermophotovoltaics (*TPV*) employing a *MIM-M* as the active element. By embedding a polar spacer dielectric and an appropriate architectural design, it is possible to enhance the light–matter interactions at high oblique incidences for *MIM-M*-based devices.

Data availability statement

All data that support the findings of this study are included within the article (and any supplementary files).

ORCID iDs

Ahmad K Jafari https://orcid.org/0000-0003-2947-7913
M D Borhan Mia https://orcid.org/0000-0003-2085-1331

References

[1] Ding F, Yang Y, Deshpande R A and Bozhevolnyi S I 2018 A review of gap-surface plasmon metasurfaces: fundamentals and applications *Nanophotonics* **7** 1129–56
[2] Matsuno Y and Sakurai A 2017 Perfect infrared absorber and emitter based on a large-area metasurface *Opt. Mat. Express* **7** 618–26
[3] Costantini D, Lefebvre A, Coutrot A-L, Moldovan-Doyen I, Hugonin J-P, Boutami S, Marquier F, Benisty H and Greffet J-J 2015 Plasmonic metasurface for directional and frequency-selective thermal emission *Phys. Rev. Applied* **4** 014023
[4] Nielsen M G, Pors A, Albrektsen O and Bozhevolnyi S I 2012 Efficient absorption of visible radiation by gap plasmon resonators *Opt. Express* **20** 13311–13319
[5] Bouchon P, Koechlin C, Pardo F, Haïdar R and Pelouard J-L 2012 Wideband omnidirectional infrared absorber with a patchwork of plasmonic nanoantennas *Opt. Lett.* **37** 1038–40
[6] Li W, Guler U, Kinsey N, Naik G V, Boltasseva A, Guan J, Shalaev V M and Kildishev A V 2014 Refractory plasmonics with titanium nitride: broadband metamaterial absorber *Adv. Mat.* **26** 7959–65
[7] Ding F, Dai J, Chen Y, Zhu J, Jin Y and Bozhevolnyi S I 2016 Broadband near-infrared metamaterial absorbs utilizing highly lossy metals *Sci. Rep.* **6** 39445
[8] Guddala S, Kumar R and Ramakrishna S R 2015 Thermally-induced nonlinear optical absorption in metamaterial perfect absorbers *Appl. Phys. Lett.* **106** 111901
[9] Liu N, Mesch M, Weiss T, Hentschel M and Giessen H 2010 Infrared perfect absorber and its application as plasmonic sensor *Nano Lett.* **10** 2342–8
[10] Ishikawa A and Tanaka T 2015 Metamaterial absorbers for infrared detection of molecular self-assembled monolayers *Sci. Rep.* **5** 1–7
[11] Zhou J, Liu X, Zhang H, Liu M, Yi Q, Liu Z and Wang J 2021 Cross-shaped titanium resonators based metasurface for ultra-broadband solar absorption *IEEE Photonic J.* **13** 1–8
[12] Khorasaninejad M and Capasso F 2017 Metalenses: versatile multifunctional photonic components *Science* **358** 1146
[13] Sriram G and Ramakrishna S A 2016 Optical limiting by nonlinear tuning of resonance in metamaterial absorbers *Opt. Lett.* **41** 5150–3
[14] Guddala S, Rao D N and Ramakrishna S A 2016 Resonant enhancement of Raman scattering in metamaterials with hybrid electromagnetic and plasmonic resonances *J. Opt.* **18** 065104
[15] Stanley R 2012 Plasmonics in the mid-infrared *Nat. Photonics* **6** 409–11
[16] Zhong Y, Malagari S D, Hamilton T and Wasserman D M 2015 Review of mid-infrared plasmonic materials *J. Nanophotonics* **9** 093791
[17] Kachiraju S R, Nekrashevich I, Ahmad I, Farooq H, Chang L, Kim S and Kim M-H 2022 Coupled surface plasmon–phonon polariton nanocavity arrays for enhanced mid-infrared absorption *Nanophotonics* **11** 4489–98
[18] Kischkat J *et al* 2012 Mid-infrared optical properties of thin films of aluminum oxide, titanium dioxide, silicon dioxide, aluminum nitride, and silicon nitride *Appl. Opt.* **51** 6789–98
[19] Vassant S, Hugonin J-P, Marquier F and Greffet J-J 2012 Berreman mode and epsilon near zero mode *Opt. Express* **20** 23971–23977
[20] Chen Y-B and Chiu F-C 2013 Trapping mid-infrared rays in a lossy film with the Berreman mode, epsilon near zero mode, and magnetic polaritons *Opt. Express* **21** 20771–85
[21] Shaykhutdinov T, Furchner A, Rappich J and Hinrichs K 2017 Mid-infrared nanospectroscopy of Berreman mode and epsilon-near-zero local field confinement in thin films *Opt. Mater. Express* **7** 3706–14
[22] Li J, Gan R, Guo Q, Liu H, Xu J and Yi F 2018 Tailoring optical responses of infrared plasmonic metamaterial absorbers by optical phonons *Opt. Express* **26** 16769–81
[23] Jafari A K, de Peralta L G and Bernussi A A 2019 *Effects of Using Lossy Materials on the Metal-Insulator-Metal (MIM) Nanostructure Absorption Spectrum the Proc. SPIE 11080, Metamaterials, Metadevices, and Metasystems*1108024
[24] Dunkelberger A D *et al* 2020 Ultrafast active tuning of the berreman mode' *ACS Photon.* **7** 279–87
[25] Khan I *et al* 2020 Engineering the Berreman mode in mid-infrared polar materials *Opt. Express* **28** 28590–9
[26] Campione S, Brener I and Marquier F 2015 Theory of epsilon-near-zero modes in ultrathin films *Phys. Rev. B,* **91** 121408 (R)
[27] Liberal I and Engheta N 2017 Near-zero refractive index photonics *Nat. Photon.* **11** 149–58
[28] Campione S, Kim I, de Ceglia D, Keeler G A and Luk T S 2016 Experimental verification of epsilon-near-zero plasmon polariton modes in degenerately doped semiconductor nanolayers *Opt. Express* **24** 18782–9
[29] Nahvi E, Liberal I and Engheta N 2020 Nonlinear metamaterial absorbers enabled by photonic doping of epsilon-near-zero metastructures *Phys. Rev. B* **102** 035404
[30] Chen J *et al* 2011 Plasmonic nickel nanoantennas *Small* **7** 2341–7
[31] https://refractiveindex.info https://refractiveindex.info/?shelf=main&book=SiO2&page=Kischkat
[32] Gunde M K 2000 Vibrational modes in amorphous silicon dioxide *Physica B* **292** 286–95
[33] Maurya K C, Bhui A, Biswas K and Saha B 2021 Anisotropic epsilon-near-pole (ENP) resonance leads to hyperbolic photonic dispersion in homologous $(Bi_2)_m(Bi_2Se_3)_n$ topological quantum materials *Appl. Phys. Lett.* **119** 011902
[34] Kats M A and Capasso F 2016 Optical absorbers based on strong interference in ultra-thin films *Laser Photon. Rev.* **10** 735–49
[35] Chevalier P, Bouchon P, Jaeck J, Lauwick D, Bardou N, Kattnig A, Pardo F and Haïdar R 2015 Absorbing metasurface created by diffractionless disordered arrays of nanoantennas *Appl. Phys. Lett.* **107** 251108
[36] Collin S 2014 Nanostructure arrays in free-space: optical properties and applications *Rep. Prog. Phys.* **77** 126402
[37] Brar V W, Jang M S, Sherrott M, Lopez J J and Atwater H A 2013 Highly confined tunable mid-infrared plasmonics in graphene nanoresonators *Nano Lett.* **13** 2541–7
[38] Brar V W, Jang M S, Sherrott M, Kim S, Lopez J J, Kim L B, Choi M and Atwater H 2014 Hybrid surface-phonon-plasmon polariton modes in graphene/monolayer h-BN heterostructures *Nano Lett.* **14** 3876–80